

Design considerations for a cascaded grating interferometer suitable for extreme ultraviolet interference lithography

Zachary H. Levine

Steven Grantham

Thomas B. Lucatorto

National Institute for Standards and Technology

100 Bureau Drive

Stop 8410

Gaithersburg, Maryland 20899-8410

E-mail: toml@nist.gov

Abstract. Recently, extreme ultraviolet interference lithography using a single grating interferometer and a highly coherent synchrotron insertion device source has proven to be an extremely useful technique for producing patterns with feature sizes in the range of 10 nm. The high demand for these nanoscale patterns and the small number of suitable highly coherent extreme ultraviolet sources has created new interest in the cascaded grating interferometer because of its relaxed demands for spatial and temporal coherence. This work extends that of earlier researchers on such systems by providing a compact algebraic analysis of the effects on fringe contrast of source divergence, spectral bandpass, lack of parallelism of the grating rulings, grating period mismatch, defocus, and wavefront curvature. The results are applied to illustrate the feasibility of implementing the interferometer on a small bending magnet synchrotron source, but the analysis should be applicable to typical portable plasma sources as well. © 2009 Society of Photo-Optical Instrumentation Engineers. [DOI: 10.1117/1.3112008]

Subject terms: extreme ultraviolet; interferometry; microlithography.

Paper 08154SSR received Sep. 29, 2008; revised manuscript received Nov. 19, 2008; accepted for publication Nov. 24, 2008; published online Apr. 10, 2009.

1 Introduction

Holographic or interference lithography has been used to make large-area periodic structures of use in many important applications. Recent examples include the nanoruler,¹ a metrological tool providing nanometer accuracy measurements over distances measured in centimeters, and an infrared negative index metamaterial.² These examples used laser light at a wavelength of 193 nm, a factor that limits the size of the smallest feature that can be patterned since two interfering beams of wavelength λ cannot produce patterns with feature sizes less than $\lambda/4$, or ≈ 50 nm in this case. More recently, Solak³ and Solak et al.⁴ have been successful in developing extreme ultraviolet-interference lithography (EUV-IL) using light at 13 nm to produce patterns with half pitches as small as 12.5 nm.

Currently, EUV-IL is performed using a single grating interferometer to recombine two parts of a highly spatially coherent beam.³ The spatial coherence requirement limits the use of the single grating instrument to synchrotron facilities with high brightness undulator sources, and only a few EUV-IL facilities are available worldwide. As it turns out, EUV-IL has proven very useful to the developers of EUV lithography in that the capability of EUV-IL to produce patterns at the 10-nm scale makes it an indispensable tool for the testing of EUV photoresists.

An interferometer based on a cascaded grating configuration can greatly reduce the requirements for spatial coherence while at the same time maintain some of the achromaticity that is characteristic of the single grating instruments. Thus, there is significant current interest in adapting the

cascaded grating interferometer to portable EUV sources so as to improve the availability of EUV-IL printing tools for use in the development of EUV resists and other applications in nanotechnology.

Anderson and Naulleau⁵ provide an excellent summary of the previous analyses of the cascaded grating system and a thorough treatment of the effects of lack of parallelism of the two gratings on performance. The present work differs in several respects by presenting a wave-vector approach that can readily provide a direct estimate of fringe visibility as a function of defocus, of deviation of the rulings from parallelism, of grating periodicity mismatch, and of spectral bandwidth.

2 Single Grating Interferometer

In the single grating system, such as that shown in Fig. 1, a collimated beam of high spatial coherence impinges on a grating with a central beam stop. The -1 diffracted order from the top section of the grating interferes with the $+1$ order beam from the bottom section of the grating to give a pattern with period $p = \lambda / (2 \sin \theta)$, a relationship determined only by the half angle θ between the two intersecting coherent beams and the wavelength λ . However, because in the bilaterally symmetric configuration as shown the grating equation implies $\theta = \sin^{-1}(\lambda / p_G)$ where p_G is the period of the grating, the pitch is given by

$$p = \lambda / (2 \sin \theta) = \lambda / (2 \lambda p_G^{-1}) = p_G / 2, \quad (1)$$

which is independent of wavelength λ , thus making the system achromatic, or in other words, insensitive to the temporal coherence of the incident beam. We note another

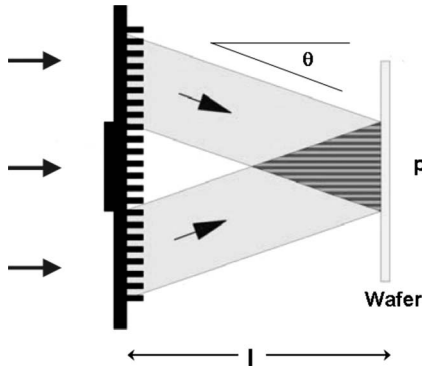


Fig. 1 Single grating interferometer, such as those used for EUV-IL, at highly coherent synchrotron sources. Wafer-coated resist is a distance ℓ from the grating. The pitch of the pattern is represented by p . A zero-order mask is shown on the grating. EUV is at normal incidence to the grating.

advantageous feature of single grating system: the pattern has half the pitch of the rulings on the grating, allowing one to make devices with feature sizes smaller than can be achieved by other forms of lithography.

The system has the disadvantage in the stringent requirements on the spatial coherence of the incident beam. This may be seen by considering a small pencil of rays at a small angle $\delta\theta_{in}$ from the (normal) incident beam. For this pencil of rays, the first-order diffracted beams are both rotated by about $\delta\theta_{in}$, which creates a box interferogram in the region of beam overlap rotated by $\delta\theta_{in}$ from the box interferogram created by the normal incidence beam. Thus, the interference pattern created by this pencil of rays at a plane at distance ℓ is shifted by $\ell \cdot \delta\theta_{in}$ from that created by the normal incidence beam, implying that maintaining fringe contrast with period p would require $\delta\theta_{in} < p/\ell$. Noting the fact that p is generally in the order of tens of nanometers and ℓ is in millimeters, we get that $\delta\theta_{in}$ must be of order tens of microradians.

3 Cascaded Grating Interferometer

An interferometer employing a second grating in a cascaded configuration can perform interference lithography with sources of only limited spatial and temporal coherence. Such a device operating at 193 nm was demonstrated in Refs. 6 and 7, and the possibility of one operating at EUV wavelengths was discussed by Wei et al.⁸ and more recently by Anderson and Naulleau.⁵

We have specialized our approach to the application to EUV-IL, where present limits on grating fabrication and source brightness are factors that restrict the choice of configuration to the geometry in which the first-order diffracted beams are used. Furthermore, we shall choose to investigate the case in which the grating G1 has pitch p_{G1} and grating G2 very close to half that pitch or $p_{G2} \approx p_{G1}/2$. (For this arrangement, the focal plane is at $z_3 \approx 2z_2$.) As was shown by Cheng et al.⁹ and other authors,^{3,5,9-12} this results in the cancellation of the first-order terms that lead to loss of fringe visibility.

In Fig. 2, we see a wavefront impinging on G1 at small angle θ_{in} . For convenience, we choose OO' to be the optic axis and define it such that the point on wavefront at O

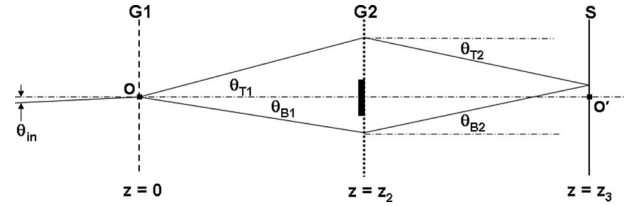


Fig. 2 Diagram showing geometry of cascaded grating interferometer.

recombines at point O' with zero phase difference between the upper and lower paths when $\theta_{in}=0$. This implies a certain relationship between the position of the rulings of G1 and those of G2 modulo p_{G2} . For the wave-vector calculations in Section 3, we choose the origin of our coordinate system at O . The grating equations give the following relationships between the different angles:

$$\theta_{T1} = \sin^{-1}(\lambda/p_{G1} + \sin \theta_{in})$$

$$\theta_{B1} = \sin^{-1}(\lambda/p_{G1} - \sin \theta_{in})$$

$$\begin{aligned} \theta_{T2} &= \sin^{-1}(\lambda/p_{G2} - \sin \theta_{T1}) \\ &= \sin^{-1}[\lambda(1/p_{G2} - 1/p_{G1}) - \sin \theta_{in}] \end{aligned}$$

$$\begin{aligned} \theta_{B2} &= \sin^{-1}(\lambda/p_{G2} - \sin \theta_{B1}) \\ &= \sin^{-1}[\lambda(1/p_{G2} - 1/p_{G1}) + \sin \theta_{in}]. \end{aligned} \quad (2)$$

We note that when $\theta_{in}=0$ and $2p_{G2}=p_{G1}$, we have that $\theta_{T1}=\theta_{B1}=\theta_{B2}=\theta_{T2}$ and the pitch of the pattern is given by

$$p = \lambda/(2 \sin \theta_{T2}) = p_{G2} \quad (3)$$

(i.e., the pitch of the pattern is the same as that of G2). A geometric argument can also be used to show that for this configuration the pattern is unchanged in the focal plane $z_3=2z_2$ for angles $\theta_{in} \neq 0$, but that a phase difference for different values of θ_{in} quickly accumulate as one departs from the focal plane (defocus).

3.1 Scalar Diffraction Analysis of the Cascaded Grating Interferometer

Our method is equivalent to the earlier approaches used to estimate the optical performance of the cascaded grating interferometer.^{5,9-12} The earlier approaches considered the phases arising from free space propagation by considering the length traversed by rays passing through the optical system as well as the phase imparted by the grating. We consider plane wave solutions to the Helmholtz equation and treat the effect of the grating (“grating phase”⁵) by addition of a wave vector of length $k_i=2\pi/p_{Gi}$ in the direction perpendicular to the grating rulings to the propagation vector of length $k=2\pi/\lambda$. We feel that vector addition of wave-vector components is conceptually simpler than considering changes in angles of the rays, which involves trigonometric and inverse trigonometric functions as seen, for example, in Eq. (2).

Consider the two-level cascaded grating shown in Fig. 2. We define coordinate axes such that the x - and y -axis are in

the plane of grating G1 with the y -axis parallel to the rulings and with the z -axis perpendicular to G1 and pointing in the direction of the light propagation. G1 is at position $z=0$, G2 is at position z_2 and screen S is at position z_3 . In the ideal case in which the pitch of G2 is half that of G1,

$$z_3 = 2z_2. \quad (4)$$

We consider the two regions of grating of G2 to be perfectly matched. We also assume G1 and G2 to have negligible thickness and the plane of G1 parallel to that of G2. Recently, the problem of a tilt of the plane of G2 out of the plane parallel to G1 has been investigated;⁵ the treatment shows that for a small range of incident angles, say $|\theta_{in}| \leq 10$ mrad, the parallelism tolerance can be readily achieved in practice. In this section, in addition to studying the effect of source size and spectral bandwidth on depth of focus, we will study two complementary problems: the case of parallel rulings with a small mismatch of the pitch from a 2:1 ratio and the rotation of the rulings of G2 relative to G1 in the case in which the pitch has a 2:1 ratio.

We consider then the propagation of a single plane wave. Before arriving at G1, it is characterized by the field

$$U^{(0)}(\vec{r}) = U_0 e^{i\vec{k} \cdot \vec{r}}, \quad (5)$$

where \vec{k} has a substantial component in the \hat{z} direction. We model the gratings and account for the grating phase by saying their effect is to multiply $U(\vec{r})$ by the factor $t_j e^{\pm i\vec{k}_j \cdot \vec{r}}$ for $j=1,2$ on the gratings G1 and G2, respectively; here \pm refers to the diffraction order ± 1 , respectively. The superscript refers to the domain: 0 being to the left of G1; 1 extending from G1 to G2; and 2 extending from G2 to S.

We consider the phase exiting G1 first. In two dimensions, the wave is described by

$$U_{\pm}^{(1)}(x,y,0) = U_0 e^{ik_x x} e^{ik_y y} t_1 e^{\pm ik_{1x} x}. \quad (6)$$

The \pm symbol refers to the two relevant diffracted beams, and t_1 is the diffraction efficiency of the first grating (assumed to be the same for the \pm first order). The value for k_x is given by $k_x = k \sin \theta_{in}$, where θ_{in} is the angle between the propagation direction and the y - z plane. Similarly, $k_y = k \sin \psi_{in}$ where ψ_{in} is the angle between the propagation direction and the x - z plane.

The Helmholtz equation constrains the free-space wave vector to be

$$k^2 = k_x^2 + k_y^2 + k_z^2 = \left(\frac{2\pi}{\lambda} \right)^2. \quad (7)$$

For this paragraph only, the symbols are generic (i.e., refer to any region of space). We assume that the waves propagate toward positive z ; thus,

$$k_z = (k^2 - k_x^2 - k_y^2)^{1/2} \quad (8)$$

(i.e., the sign of k_z is specified).

In the region between G1 and G2, the waves are given by

$$U_{\pm}^{(1)}(x,y,z) = U_1 e^{i(k_x \pm k_{1x})x} e^{ik_y y} e^{i[k^2 - (k_x \pm k_{1x})^2 - k_y^2]^{1/2} z}, \quad (9)$$

introducing $U_1 = U_0 t_1$. Equation (9) is valid in particular at the entrance face of the second grating (i.e., with $z=z_2$). The grating G2 will impart a factor $t_2 e^{\mp ik_{2x} x \pm ik_{2y} y}$ to the impinging waves. In the case when the rulings of G2 are parallel to those of G1 (and therefore to the y -axis), $k_{2y} = 0$ and $k_{2x} = 2\pi/p_{G2}$.

At the exit face of G2, the waves are given by

$$U_{\pm}^{(2)}(x,y,z_2) = U_1 e^{i(k_x \pm k_{1x})x} e^{ik_y y} e^{i[k^2 - (k_x \pm k_{1x})^2 - k_y^2]^{1/2} z_2} t_2 e^{\mp ik_{2x} x \pm ik_{2y} y}. \quad (10)$$

Equation (10) is derived by setting z to z_2 and multiplying by the factor associated with the \mp first-order diffraction grating from G2. The sign \pm on the ik_{1x} term on G1 is matched with \mp on the term $ik_{2x} x$ on G2 to describe those waves that bend inward to interfere on the sample S. Using the same argument as before, the waves at a general point of region 2 are given by

$$U_{\pm}^{(2)}(x,y,z) = U_2 e^{i(k_x \pm k_{1x} \mp k_{2x})x} e^{i(k_y \pm k_{2y})y} e^{i[k^2 - (k_x \pm k_{1x})^2 - k_y^2]^{1/2} z_2} \times e^{i[k^2 - (k_x \pm k_{1x} \mp k_{2x})^2 - (k_y \pm k_{2y})^2]^{1/2} (z-z_2)}, \quad (11)$$

introducing $U_2 = U_1 t_2 = U_0 t_1 t_2$.

The two waves described by Eq. (11) interfere in region 2, including the plane $z=z_3$. The intensity pattern is described by

$$I(x,y,z) = \frac{1}{2} \left| \sum_{\pm} U_{\pm}^{(2)}(x,y,z) \right|^2. \quad (12)$$

The intensity may be written as a sum of two terms

$$I(x,y,z) = I^{(1)}(x,y,z) + I^{(2)}(x,y,z). \quad (13)$$

There is a background term

$$I^{(1)}(x,y,z) = |U_2|^2 \quad (14)$$

and an interference term

$$I^{(2)}(x,y,z) = |U_2|^2 \text{Re}(e^{i(2k_{1x} - 2k_{2x})x} e^{i2k_{2y}y} e^{i\phi}), \quad (15)$$

where R stands for the real part and

$$\phi = \sum_{\pm} \pm [k^2 - (k_x \pm k_{1x})^2 - k_y^2]^{1/2} z_2 \pm [k^2 - (k_x \pm k_{1x} \mp k_{2x})^2 - (k_y \pm k_{2y})^2]^{1/2} (z - z_2). \quad (16)$$

3.2 Calculation of Depth of Field for a Given Angular Dispersion and Spectral Bandwidth of the Input Illumination

Equation (15) will be the starting point for a few special cases. First, we consider the perfectly aligned cascaded grating characterized by $k_{2x} = 2k_{1x}$ (physically, the pitch of G1 is twice that of G2) and use $z_3 = 2z_2 + \delta_z$ with the understanding that δ_z will be small. The interference term becomes

$$I^{(2)}(x, y, z) = |U_2|^2 \text{Re} \left(e^{-2ik_{1x}x} \prod_{\pm} e^{\pm i[k^2 - (k_x \mp k_{1x})^2 - k_y^2]^{1/2} \delta_z} \right). \quad (17)$$

Next, we assume that $k'^2 \equiv k^2 - k_y^2 \gg k_x^2, k_{1x}^2$, introducing $k' > 0$. A Taylor expansion of Eq. (17) leads to

$$I^{(2)}(x, y, z) = |U_2|^2 \text{Re} \left(e^{-2ik_{1x}x} e^{2ik_x k_{1x} / k' \delta_z} \right) \quad (18)$$

to the lowest nonvanishing order.

We shall use Eq. (18) to make some general statements about the behavior of the interferometer for the cases in which the inequality $k^2 - k_y^2 \gg k_{1x}^2$ holds. There is a sinusoidal variation in the interference term with x whose wavelength is independent of the incident beam parameters. The phase, however, does depend on the beam parameters (except for $\delta_z = 0$) through the dimensionless parameter

$$\alpha \equiv \frac{k_x}{k'} = \frac{k_x}{(k^2 - k_y^2)^{1/2}}, \quad (19)$$

defining α . Typically, we expect $k_y \ll k$, so α depends in first order on variations in k_x but only second order on small k_y . We also note that variations in λ (or therefore k) do not affect α in general, because since the angular dispersion of most illumination schemes will be determined by geometrical factors so that both $k_x \sim k$ and $k_y \sim k$. Note that $k_{1x} \delta_z$ is another dimensionless parameter; thus, the depth of field will scale linearly with the grating pitch $p_{G1} = 2\pi/k_{1x}$, a property noted by Cheng et al.⁹ and others.

According to Eq. (18), for any given incident beam parameters, there is a sinusoidal pattern. However, as the incident beam parameter α varies, this sinusoidal pattern shifts in space for nonzero δ_z . To determine the fringe visibility $V(\delta_z)$, we must average the interference pattern over a distribution of α . Given a normalized probability distribution $f(\alpha)$,

$$\bar{I}^{(2)}(x, y, \delta_z) = I^{(1)} \text{Re} \left[e^{-2ik_{1x}x} \int d\alpha f(\alpha) e^{2ik_x k_{1x} \delta_z \alpha} \right] \quad (20)$$

, is the appropriate average. Assume that $f(\alpha)$ is a normalized Gaussian with standard deviation σ_α and mean α_0 , i.e.,

$$f(\alpha) = \frac{1}{\sqrt{2\pi}\sigma_\alpha} \exp \left[-\frac{(\alpha - \alpha_0)^2}{2\sigma_\alpha^2} \right]. \quad (21)$$

(A nonzero α_0 would arise if the beam has a nonzero average k_x , i.e., physically, if the beam is not at normal incidence on average.) The integral is elementary. The result is

$$\bar{I}^{(2)}(x, y, z) = I^{(1)} e^{-2\sigma_\alpha^2 k_{1x}^2 \delta_z^2} \cos[2k_{1x}(\delta_z \alpha_0 + x)]. \quad (22)$$

Hence, the visibility has the functional dependence

$$V(\delta_z) = \frac{I_{\max} - I_{\min}}{I_{\max} + I_{\min}} = e^{-2\sigma_\alpha^2 k_{1x}^2 \delta_z^2}, \quad (23)$$

i.e., the maximum and minimum of $I = I^{(1)} + \bar{I}^{(2)}$ are taken over x for fixed δ_z .

If we choose a minimum acceptable value for the fringe visibility V_{\min} , typically 0.5–0.8, then

$$|\delta_z| \leq \frac{1}{\sqrt{2}\sigma_\alpha k_{1x}} \left(\ln \frac{1}{V_{\min}} \right)^{1/2} \quad (24)$$

in the region of visible fringes. Without loss of generality, we take $k_{1x} > 0$. The dependence on V_{\min} is quite weak.

For the purpose of illustration, we shall suppose all of the variation in α is due to Gaussian variation in k_x around the value $k_x = 0$ with standard deviation σ_{k_x} ; thus, $k = 2\pi/\lambda$ is fixed and $k_y = 0$. We choose to have $V_{\min} = 0.5$. From the definition of α , given in Eq. (19), $\sigma_{k_x} = \sigma_\alpha (k^2 - k_y^2)^{1/2}$, or simply $\sigma_{k_x} = \sigma_\alpha k$ for $k_y = 0$. In this case,

$$|\delta_z| \leq 0.5887 \frac{k}{\sigma_{k_x} k_{1x}} = 0.5887 \frac{p_{G1}}{\lambda \sigma_{k_x}}. \quad (25)$$

We are interested in the EUV case of $\lambda = 13.5$ nm and $p_{G1} = 50$ nm, which yields a 12.5 nm half pitch on the sample. In this case,

$$|\delta_z| \leq 2.2 \frac{1}{\sigma_{k_x}} \approx 0.35 \frac{\lambda}{\sigma_{\theta_{\text{in}}}}. \quad (26)$$

In making the final approximate equality, the small-angle approximation $k_x \ll k$ has been invoked and, in this case, $\sigma_{\theta_{\text{in}}}$ represents the divergence of the beam as measured in the x - z plane. Thus, there is a trade-off between the acceptance angle for incident radiation θ_{in} and the depth of field $2\delta_z^{(\max)}$. To end with a fully numerical example, if $\sigma_{\theta_{\text{in}}} = 10$ mrad and the spectral bandwidth is characterized by $\Delta\lambda = 1.0$ nm, which is roughly characteristic of beam line 1 of the bending magnet source at the Synchrotron Ultraviolet Research Facility (SURF III) of the National Institute of Standards and Technology (NIST), then the depth of field is 0.9 μm . (The spectral bandwidth is determined by the fact that the synchrotron radiation from the bending magnet source is reflected by two normal incidence multilayer mirrors. At the level of our approximation, this relatively small bandwidth does not affect the depth of field.)

For more detail, we have plotted in Fig. 3 the fringe visibility as a function of defocus by evaluating the approximation represented by Eq. (23) and compared that value to the more precise value obtained by numerical integration of the phase in Eq. (16) over the distribution given in Eq. (21). As can be seen, the approximation works quite well for $p_{G1} = 50$ nm (or $k_{1x}^2/k^2 \approx 0.07$).

3.3 Calculation of Fringe Contrast in the Case of Grating Pitch Mismatch

Next, we return to Eq. (16) and seek the location of the sample plane that leads to the best interference pattern. Specifically, introducing δk_{2x} via $k_{2x} = 2k_{1x} + \delta k_{2x}$, we want to adjust z_3 so that a particular phase vanishes, i.e.,

$$\sum_{\pm} \pm [k^2 - (k_x \pm k_{1x})^2 - k_y^2]^{1/2} z_2 \pm [k^2 - (k_x \mp k_{1x} \mp \delta k_{2x})^2 - (k_y \pm k_{2y})^2]^{1/2} (z_3 - z_2) = 0. \quad (27)$$

The solution is

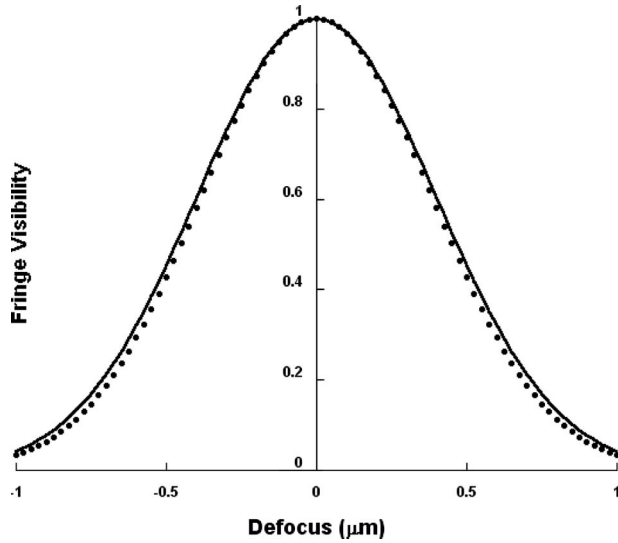


Fig. 3 Fringe visibility for the case of $\sigma_{\theta_{in}}=10$ mrad with a $p_{G1}=50$ nm and $p_{G2}=25$ nm grating pair as a function of defocus. The solid line is from the function in Eq. (23), and the dots are from numerical integration of the phase in Eq. (16) over the distribution given in Eq. (21).

$$z_3 = z_2[1 - N/D] \quad (28)$$

with

$$N = \sum_{\pm} \pm [k^2 - (k_x \pm k_{1x})^2 - k_y^2]^{1/2} \quad (29)$$

and

$$D = \sum_{\pm} \pm [k^2 - (k_x \mp k_{1x} \mp \delta k_{2x})^2 - (k_y \pm k_{2y})^2]^{1/2}. \quad (30)$$

For the ideal case, $\delta k_{2x}=0$ and $k_{2y}=0$ (i.e., no pitch mismatch and the rulings of G2 parallel to those of G1), we recover the well-known result $z_3=2z_2$ (i.e., the distance from G1 to the sample plane is twice the distance from G1 to G2). If the rulings are parallel but not necessarily with a 2:1 ratio of the pitch, then we have $k_{2y}=0$ and δk_{2x} small (for the cases of interest here). In this case, we may reintroduce $k'^2=k^2-k_y^2$, and it may be seen in Eq. (16) that the effect of a y component of the incident beam is no different from an increase in the wavelength λ . For our application, the range of wavelength is a few percent of the wavelength itself, whereas the maximum expected incident angles are, at most, 5 mrad, which is represented by $k_y \approx 0.005k$. Because this term enters k' in second order but the wavelength variation enters in first order, we may neglect the y component of the incident angle as its contribution to the loss of fringe visibility is dwarfed by that of the bandwidth in wavelength.

To explore the effects of grating mismatch with $k_{2y}=0$ (parallel rulings), we perform a Taylor expansion to the lowest nonvanishing order in the quantities: $k_x^2/(k^2-k_{1x}^2)$, $\delta k_{2x}/(k^2-k_{1x}^2)^{1/2}$, and $k_{2x}/(k^2-k_{1x}^2)^{1/2}$ to obtain the expres-

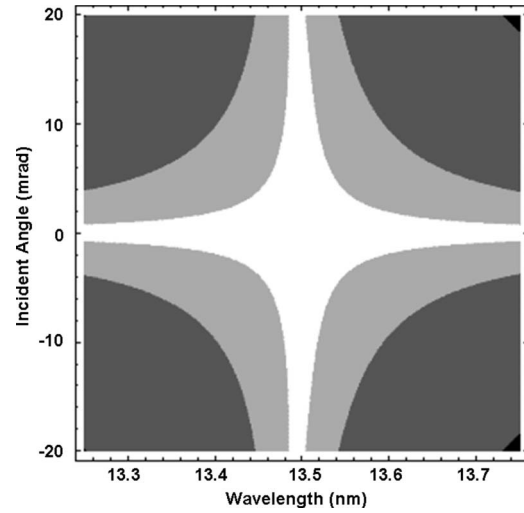


Fig. 4 Phase given by Eq. (16) as a function of the wavelength of the incident light and the angle of incidence in the x - z plane. The rulings are assumed to be parallel to the y -axis. The pitch of first grating is $p_{G1}=50$ nm, and δk_{2x} is set to 1% of k_{1x} , which corresponds to a pitch of the second grating of $p_{G2}=24.88$ nm. The boundary between the white and light gray regions represents a phase shift of $\pi/50$ of either sign compared to a 0 phase in the center of the plot. The boundary between the light gray and dark gray regions represents a phase shift of $\pi/10$ and, between the dark gray and black, $\pi/2$. The spacing between the first grating and the second grating is 10 mm, and the spacing between the second grating and the image plane is taken to be 9.8932 mm, which is the solution to Eq. (28) for $k_x=k_y=0$ and $\lambda=13.5$ nm.

$$z_3 - z_2 = z_2 \left[1 - \frac{\delta k_{2x}}{k_{1x}} \left(\frac{k^2}{k^2 - k_{1x}^2} \right) + \frac{\delta k_{2x} k_{1x} k_x^2}{2(k^2 - k_{1x}^2)^2} \right]. \quad (31)$$

The key points of this expansion are: (i) it is possible to shift the focus to compensate for a grid mismatch and (ii) the focus is no longer independent of the angle of incidence. In a typical case, the depth of field is $\sim 1 \mu\text{m}$ and the spacing z_2 is 10 mm. This dependence is expressed by the third term in the brackets and may be easily evaluated for various values of the parameters. In practical cases where $\delta k_{2x}/k_{1x}$ and k_x/k are each on the order of a percent, this variation is on the order of $0.1 \mu\text{m}$, which is a small part of the depth of focus.

In Fig. 4, we show a plot of lines of equal phase of $\pi/50$, $\pi/10$, and $\pi/2$ in the focal plane determined by Eq. (31) for a 1%-pitch mismatch as a function of wavelength and incident angle. To get an idea of the depth of field, we have plotted the same quantities for a position 500 nm from the focal plane in Fig. 5. As can be seen, a small amount of pitch mismatch decreases the tolerance in input angle and bandwidth for the interferometer.

3.4 Calculation of Depth of Field for Case of Matched Gratings in Parallel Planes with Ruling Directions Not Parallel

As a final nonideal case, we consider the grid bars rotated with respect to each other by an angle ψ . The rulings of G1 are taken to be parallel to the y -axis. The phase in the sample plane is given by Eq. (16), with $k_{2x}=(2\pi/p_{G2})\cos\psi$ and $k_{2y}=(2\pi/p_{G2})\sin\psi$. The change in

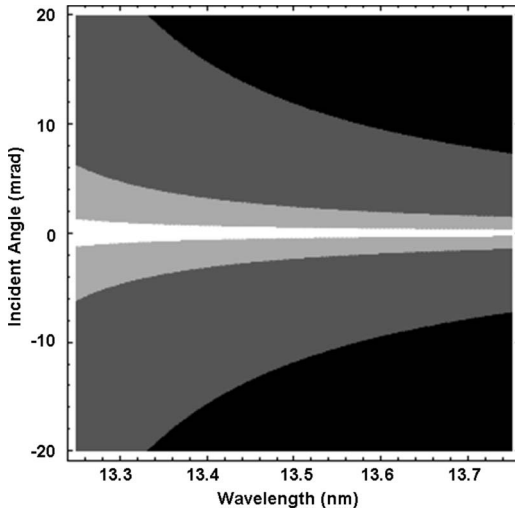


Fig. 5 Same plot as Fig. 4, but the spacing between the second grating and the image plane is increased by 500 nm, to 9.8937 mm. Fringe visibility is reasonably high if the black region is avoided.

the focal plane and the maximum phase deviations for typical mismatch angles are given in Tables 1 and 2. As can be seen, a modest alignment deviation ψ results in a negligible change in the focal plane distance. The variation in z_3 over the expected bandwidth from 98% to 102% of the central wavelength of 13.5 nm is <1 nm, also a negligible amount. When the maximum deviation of the incident phase exceeds π by a significant amount, the fringe visibility becomes vanishingly small. Tables 1 and 2 indicate acceptable and unacceptable conditions.

We conclude that the alignment of the gratings is critical. In the case of aligned gratings with a slightly mismatched pitch, it is possible to compensate by adjusting the spacing between the second grating and the sample plane to achieve a robust implementation. However, errors in alignment lead to phase errors even at ideal z and to a smaller depth of field. If the alignment required by Tables 1 and 2 cannot be achieved, one option for the designer would be to

Table 1 The range of the phase that is introduced by a “clocking error” (i.e., by nonparallelism of the gratings G1 and G2 by an angle ψ). The second column is the ideal position at the central wavelength of 13.5 nm for gratings with pitches of 100 and 50 nm, respectively, with a G1 to G2 spacing of 10 mm. The third column gives the biggest phase difference introduced at the sample plane over the range $13.25 \leq \lambda \leq 13.75$ nm at the ideal sample position and the fourth column at $1 \mu\text{m}$ past the ideal position to provide a measure of the depth of focus. A maximum half-angle of 5 mrad in x and 5 mrad in y was assumed.

ψ (μrad)	$z_3 - 2z_2$ (nm)	ϕ/π (ideal z)	ϕ/π (ideal $z+1 \mu\text{m}$)
0	0	0	0.404
25	0.025	0.202	0.606
50	0.049	0.404	0.808
100	0.098	0.808	1.212

Table 2 Same as Table 1 but for gratings with pitches of 50 and 25 nm, respectively, with the fourth column now representing a position $0.5 \mu\text{m}$ past the ideal. Note the linear dependence on ψ and the offset in z in this table and in Table 1.

ψ (μrad)	$z_3 - 2z_2$ (nm)	ϕ/π (ideal z)	ϕ/π (ideal $z+0.5 \mu\text{m}$)
0	0	0	0.416
25	0.031	0.416	0.832
50	0.062	0.832	1.248
100	0.124	1.664	2.080

reduce the spacing z_2 between the two gratings because the phase error is proportional to this spacing or to reduce the angular dispersion of the incoming light. The ability to align the gratings may ultimately determine the maximum size of the device and the acceptable divergence of the input radiation.

Certain relevant cases have been given in Tables 1 and 2. For estimations, it may be possible to scale these answers. For example, Eq. (28) shows that $z_3 \sim z_2$. Returning to Eq. (16), if we set $z = z_3$, for some choice of the set of parameters $k, k_x, k_{1x}, k_{2x}, k_y,$ and k_{2y} , it may be seen that the phase for some other values for the parameters [and hence the phase error, given that Eq. (16) sets the phase to zero] is proportional to z_2 . Thus, reducing z_2 will proportionately reduce the phase error at the expense of limiting the maximum field size. [The phase equal to the phase error, given that Eq. (27) sets the phase to zero.] The depth of field, however, is independent of z_2 . Although the Taylor expansions are somewhat involved, numerically the phase error is proportional to both k_x and k_y , and similar to the case of the grating mismatches, the dependence on λ is quite weak.

4 Effect of Spherical Waves

4.1 Treatment of Spherical Waves

In describing the operation of the interferometer, we have thus far used an approximation with plane waves. In an application using a source at a finite distance, we must take into account that the wavefronts are not planar but are better approximated as spherical wavefronts. The use of spherical waves will change the fringe visibility as one moves from the optic axis along the focal plane.

For simplicity, we treat the case where $\theta_{\text{in}} = 0$ so that $\theta_{T1} = \theta_{B1} = \theta$ and $z_3 = 2z_2$. We consider in Fig. 6 a point A in the focal plane. The spherical wave front with arc AC_{TS} , approximated by plane wave represented by AC_T interferes with spherical wavefront AC_{BS} approximated by AC_B at A . The phase difference between the upper and lower beams in the plane wave approximation is $2AO'(2\pi/\lambda)\sin\theta$, whereas in the spherical wave case the phase difference is $(2\pi/\lambda)(R_+ - R_-)$, where R_+ is the radius of the spherical wave associated with AC_{BS} and R_- that associated with AC_{TS} . Thus, to determine the change introduced by the spherical wavefronts, we must evaluate the difference between these two phase differences.

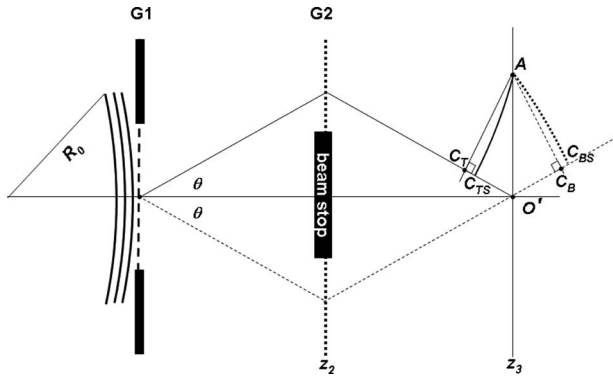


Fig. 6 Diagram showing elements used in estimating the effect of wavefront curvature.

If we make the further simplifying assumption that the radii of curvature of the wavefronts are just the optical path lengths from the source, then given the geometric relationships between the chords $AC_T=AO' \cos \theta=AC_B$ and radii of curvature (which we have called R_+ and R_-), and the apothems ($R_0+2z_2/\cos \theta \pm AO' \sin \theta$), we get the following relationships:

$$R_{\pm} = \sqrt{\left(R_0 + \frac{2z_2}{\cos \theta} \pm AO' \sin \theta\right)^2 + (AO' \cos \theta)^2}. \quad (32)$$

Using Eq. (32), one can solve for the difference between R_+ and R_- to yield the path difference between the two wavefronts. This path difference can then be compared to the path difference in the plane-wave case, which is equal to $2AO' \sin \theta$, and thus, the phase difference at position A is given by

$$\phi_A = (2\pi/\lambda)[(R_+ - R_-) - 2AO' \sin \theta]. \quad (33)$$

4.2 Effect of Spherical Wavefront and Estimation of Exposure Times at SURF III

Finally, we shall specifically consider the case of an existing synchrotron radiation source. The SURF III is a storage ring located at NIST's Gaithersburg campus. SURF III is a single-magnet circular electron storage ring with an 838-mm radius. The vertical electron beam size can be varied from about 1 to 3.5 mm full width half-maximum. A design for a dedicated beamline for EUV-IL at SURF III has been proposed. This design incorporates a near-normal incidence (0.5 deg) multilayer optic to create a 1:1 image of the electron beam and planar 45-deg angle of incidence mirror to relay the image into the interferometer chamber. Keeping the imaging optic at a near-normal incidence will reduce the spherical aberration, astigmatism, and coma in the system. We have modeled the output of the proposed system using Zemax ray-tracing software.¹³

In the model, we considered incorporating a 3 m radius of curvature spherical optic with a diameter of 75 mm. The optic was placed 3 m away from the source. This configuration is somewhat similar to another beamline at SURF III that incorporates a single focusing mirror with a 10-deg angle of incidence. We used data from that beam line to determine that a multilayer at a 3-m distance from SURF III will collect and image 6.2 mW of in-band power. The in-band image power will be reduced to 3.2 mW by the 45-deg folding mirror. The intensity pattern was modeled at plane 100 mm after the image plane of the optical system. The result of the model is shown in the intensity pattern in Fig. 7.

Next, we considered a cascaded grating with a with single grating efficiency in the ± 1 orders of $\approx 7\%$. This yields a throughput of $\approx 1\%$ at the wafer plane. This yields an intensity of approximately $30 \mu\text{W}/\text{mm}^2$ or $3 \text{ mW}/\text{cm}^2$. This yields an exposure time for a $100\text{-mJ}/\text{cm}^2$ resist of $\approx 35 \text{ s}$.

Furthermore, consider the following parameters for a

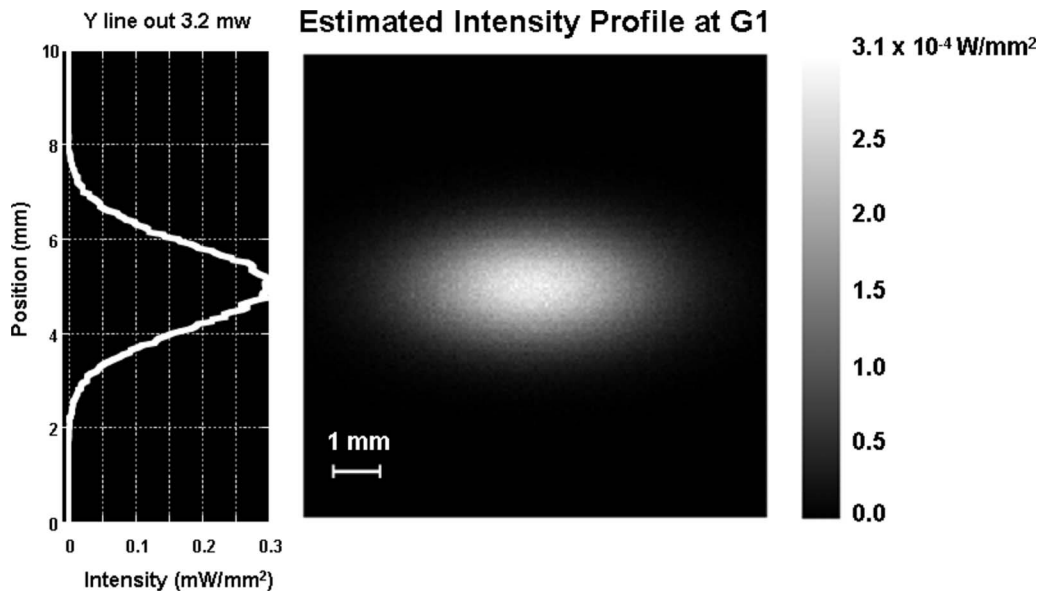


Fig. 7 Estimated intensity profile at the grating G1. SURF III operating with a beam current of 300 mA and a vertical height of 1.5 mm.

proposed EUV cascaded grating system: $\lambda=13.5$ nm, $p_{G1}=50$ nm, $p_{G2}=25$ nm, $z_2=10$ mm, $R_0=100$ mm, and $AO'=0.5$ mm.

From Section 4, we can consider the spherical wavefront produced under these conditions. The result is a plane-wave propagation difference of $270.000 \mu\text{m}$ and a spherical wave path difference of $269.998 \mu\text{m}$. Therefore, the path difference is 2 nm. This shows that the interference pattern generated in the spherical wave case is nearly identical in phase to the plane-wave case and setting our interferometer 100 mm from the focus is adequate to achieve a uniform interference pattern over a 1.0-mm field. An interferometer test bed has been designed and constructed for demonstration experiments at SURF III. This interferometer has been tested in order to determine the thermal and mechanical stability of the device. These tests have shown that the test-bed performs adequately for exposure times on the order of a few minutes.¹⁴

5 Conclusions

In the ideal configuration for EUV-IL, namely, the use of first-order diffracted beams with $p_{G2}=p_{G1}/2$, rulings perfectly aligned, and $z_3=z_2$, the depth of focus depends most strongly on beam divergence perpendicular to the rulings (i.e., θ_{in}). We have shown that in this ideal case the depth of focus is given by $0.6 p_{G1}/\sigma_{\theta_{in}}$, where $\sigma_{\theta_{in}}$ characterizes the Gaussian width of the beam divergence.

If the gratings are ruled by an electron-beam writer, the average pitch mismatch can be made to be 1% or less.¹⁵ With a pitch mismatch of 0.5% in the case of $p_{G1}=50$ nm, we see from Figs. 4 and 5 that there is a wavelength dependence of the phase and some decrease in the depth of focus.

The most critical element in the construction of the interferometer is the alignment of the rulings of G1 with those of G2. We have shown that a modest mismatch of the orientation of the two gratings can lead to a serious degradation in the performance of the cascaded interferometer and may limit the size or the acceptable divergence of the input.

Acknowledgments

The authors extend special appreciation to Harun Solak, J. Alexander Liddle, Ryan Vallance, Kenan Cole, and Ted Bloomstein for many helpful suggestions on theory and design elements, and thank Mordechai Rothschild, Franco Cerrina, and Tom McIlrath for very fruitful discussions.

References

1. P. Konkola, C. Chen, R. K. Heilman, C. Joo, J. Montoga, C.-H. Chang, and M. L. Schattenburg, "Nanometer-level repeatable metrology using the Nanoruler," *J. Vac. Sci. Technol. B* **21**, 3097 (2003).
2. S. Zhang, W. Fan, N. C. Panoiu, K. J. Malloy, R. M. Osgood, and S. R. Brueck, "Experimental demonstration of a near-infrared negative-index metamaterial," *Phys. Rev. Lett.* **95**, 137404 (2005).
3. H. H. Solak, "Topical Review: Nanolithography with coherent extreme ultraviolet light," *J. Phys. D* **39**, R171 (2006).
4. H. H. Solak, Y. Ekinici, and P. Kauser, "Photon-beam lithography reaches 12.5 nm half pitch resolution," *J. Vac. Sci. Technol. B* **25**, 91 (2007).
5. C. N. Anderson and P. P. Naulleau, "Tilt sensitivity of the two-grating interferometer," *Appl. Opt.* **47**, 1327 (2008).
6. A. Yen, E. H. Anderson, R. A. Ghanbari, M. L. Schattenburg, and H. I. Smith, "Achromatic holographic configuration for 100-nm period lithography," *Appl. Opt.* **31**, 4540 (1992).
7. T. A. Savas, M. L. Schattenburg, J. M. Carter, and H. I. Smith, "Large-area achromatic interferometric lithography for 100-nm period gratings and grids," *J. Vac. Sci. Technol. B* **14**, 4167 (1996).
8. M. Wei, D. T. Attwood, T. K. Gustafson, and E. H. Anderson, "Patterning a 50-nm period grating using soft X-ray spatial frequency multiplication," *J. Vac. Sci. Technol. B* **12**, 3648 (1994).
9. B. J. Chang, R. Alferness, and E. N. Leith, "Space-invariant achromatic grating interferometers: theory," *Appl. Opt.* **14**, 1592 (1975).
10. Y.-S. Cheng, "Temporal coherence requirements in a symmetric-path interferometer," *Appl. Opt.* **36**, 800 (1997).
11. Y.-S. Cheng, "Fringe formation in incoherent light with a two-grating interferometer," *Appl. Opt.* **23**, 3057 (1984).
12. G. J. Swanson, "Broad-source fringes in grating and conventional interferometers," *J. Opt. Soc. Am. A* **1**, 1148 (1984).
13. Identification of certain commercial items does not imply a recommendation or endorsement by NIST nor does it imply that the items are the best available for the purpose.
14. K. Cole, R. R. Vallance, and T. Lucatorto, "Design of an interferometer for EUV interference lithography at the NIST SURF III Synchrotron," in *Proc. of the Am. Soc. for Precision Eng.'s Spring Topical Meeting on Precision Mechanical Design & Mechatronics for Sub 50 nm Semiconductor Equipment*, Berkeley, CA, April 7-8 2008
15. J. Alexander Liddle, personal communication.



Zachary H. Levine obtained his SB in mathematics and one in physics from MIT in 1976. He obtained his PhD from the University of Pennsylvania in 1983. He has been a physicist with the National Institute of Standards and Technology since 1994 and became a fellow of the American Physical Society in 2001. His research interests include optical and electron probes of matter and tomography. He has 75 peer-reviewed publications, three U.S. patents, and two cartoons in *APS News*.



Steven Grantham received his PhD from the University of Central Florida's Center for Research and Education in Optics and Lasers (CREOL). His graduate research involved the study and application of short pulse laser-produced plasmas. Since 1999, he has worked at NIST with an emphasis on EUV metrology for EUV lithography applications. In 2004, he received the Department of Commerce silver medal for his role in the development of NIST's EUV metrology program.



Tom Lucatorto received his Ph.D. from Columbia for work in atomic structure. He is a fellow of the American Physical Society and the recipient of the Department of Commerce Silver Medal. He has been the leader of the Photon Physics Group at NIST for the last two decades. That group initiated a program in EUV metrology in 1989 to aid in characterizing the EUV optics for astronomy, fusion plasma diagnostics, laser development, and the original AT&T program to explore EUV lithography as a possible next-generation lithography.